PHYSICAL REVIEW B **108**, 035133 (2023)

Raman signatures of quadratic band touching state and strong spin-phonon coupling in pyrochlore iridates $(Sm_{1-x}Bi_x)_2Ir_2O_7$

M. Rosalin,[1] Prachi Telang,[2] Surjeet Singh,[2] D. V. S. Muthu,[1] and A. K. Sood[1,*]

[1]*Department of Physics, Indian Institute of Science, Bangalore 560012, India*

[2]*Department of Physics, Indian Institute of Science Education and Research, Pune, Maharashtra 411008, India*

(Received 12 April 2023; revised 9 June 2023; accepted 6 July 2023; published 18 July 2023)

In this work, we report low-temperature Raman spectroscopic measurement to investigate the temperature dependence of phonons and magnetic as well as electronic excitations in $(Sm_{1-x}Bi_x)_2Ir_2O_7$ for $x = 0$, 0.02, 0.035, 0.05, and 0.10. A strong spin-phonon coupling induced phonon renormalization is observed below magnetic transition temperature T_N for samples with $x \leqslant 0.035$. An underlying broad continuum attributed to pronounced spin-spin correlations is observed below T_N for pure $Sm_2Ir_2O_7$. Significant phonon anomalies at lower temperatures, much below T_N, for $x = 0$ and 0.02, are observed and are attributed to a possible crossover into the Weyl semimetal state. Most interestingly, we observe clear signatures of quadratic band touching in $x = 0.05$ and 0.10 systems in terms of a broad electronic continuum at low temperatures analyzed using the Raman susceptibility for a non-Fermi liquid, corroborating the inference from recent transport measurements.

DOI: 10.1103/PhysRevB.108.035133

I. INTRODUCTION

Strongly correlated $5d$-electron systems have opened a new pathway in condensed matter physics due to spin-orbit coupling (SOC) induced unconventional topological phases. The interplay between metal-insulator transition (MIT) and "all in–all out" (AIAO) magnetic ordering in the $5d$-pyrochlore iridates has provided a fated goal to search for the fingerprints of exotic states of matter in these geometrically frustrated systems. The $5d$ transition metal oxides (TMOs) stand at the crossroad of strongly correlated systems where the SOC and the Coulomb interaction compete at the same energy scale. In $5d$ iridates, this is further enhanced by the crystal-field interaction that splits the t_{2g} orbitals and leaves the system in a low spin state ($J_{\mathrm{eff}} = 1/2$). Among the iridates, pyrochlore iridates $A_2Ir_2O_7$ ($A =$ Y, Bi, and rare-earth elements) have attracted much attention as they potentially show various exotic phenomena and topologically nontrivial ground states [1–7]. The cubic pyrochlore structure consists of both A and Ir sublattices forming an interpenetrating corner-shared tetrahedral network that introduces geometrical frustration in the system. The SOC dominant Dzyaloshinskii-Moriya interaction competes with frustration and gives rise to an AIAO antiferromagnetically ordered ground state with broken time-reversal symmetry below T_N [1,8]. The AIAO configuration arises from iridium spins pointing into or out of the tetrahedral unit along the (1,1,1) axis of the pyrochlore lattice in an alternating fashion [1]. The physical properties evolve with A site cation radius from magnetic insulating to a complex nonmagnetic metallic behavior. The ionic radius boundary for MIT lies between Nd and Pr, where $Pr_2Ir_2O_7$ being the end member shows spin-liquid behavior and does not show any long-range magnetic order down to 0.3 K [9]. On the contrary, smaller rare-earth pyrochlore iridates such as $Gd_2Ir_2O_7$, $Tb_2Ir_2O_7$, $Dy_2Ir_2O_7$, and $Ho_2Ir_2O_7$ remain insulating at all temperatures, whereas $Nd_2Ir_2O_7$, $Sm_2Ir_2O_7$, and $Eu_2Ir_2O_7$ show MIT along with magnetic transition in the temperature range of 100–150 K [10–14]. These three candidates are theoretically proposed to host the Weyl semimetal (WSM) state at low temperatures due to the breaking of time-reversal symmetry with the preservation of requisite inversion symmetry [4,6,7]. Supportive experimental signatures in establishing a correlated WSM state for $Sm_2Ir_2O_7$ have also been provided by recent resonant elastic and inelastic x-ray scattering studies [1]. Similarly, high-pressure transport measurements on this compound also identified a low-pressure region of P-T space to host a magnetic WSM state [2]. The AIAO order is suppressed at a critical pressure $P_c = 6$ GPa, whereas the same space group retains across the quantum critical point.

$Sm_2Ir_2O_7$ is a WSM candidate with concomitant MIT and AIAO near 120 K. Application of chemical pressure, i.e., doping A^{3+} or Ir^{4+} sites, has proven an effective tool to tune the relative scale of interactions and electronic bandwidth in this class of materials. Recently, it has been reported that $Sm_2Ir_2O_7$ doped with Bi (lattice constant $a = 10.3235$ Å for $Sm_2Ir_2O_7$ and 10.3250 Å for $Bi_2Ir_2O_7$) shows anomalous lattice contraction up to 10% Bi doping and enters normal lattice expansion limit with further Bi substitution [15]. The combined magnetic, specific heat, and transport data on these systems suggest the presence of a WSM state up to 2% Bi substitution with resistivity (ρ) following $1/T$ dependence at low temperatures in agreement with theory [16]. With a further increase in Bi doping, the WSM phase is replaced by the quadratic band touching (QBT) state where the low-temperature resistivity shows $-\ln T$ dependence [15]. At the WSM-QBT boundary, there lies a crossover phase, as

---

[*] asood@iisc.ac.in

predicted by Savary *et al.* [3], with the unconventional temperature dependence of resistivity. Our present work is motivated to look for the signatures of this unconventional crossover between these topological phases and also understand the influence of MIT-coupled magnetic transition and the WSM state on the phonon self-energies in $Sm_2Ir_2O_7$ and Bi-substituted $Sm_2Ir_2O_7$ samples up to 75% isovalent Bi substitution, concentrating more on the low doping concentration regime.

II. EXPERIMENTAL DETAILS

All the samples in the series $(Sm_{1-x}Bi_x)_2Ir_2O_7$ ($x = 0$, 0.02, 0.035, 0.05, 0.1, 0.25, 0.50, and 0.75, were synthesized via a solid-state reaction method using a high-purity (better than 99.9%) form of precursors of Sm_2O_3, IrO_2, and Bi_2O_3. Here x refers to the nominal composition, which is the same as the measured value determined using an energy dispersive x-ray analysis and Rietveld refinement of the synchrotron powder x-ray diffraction. The details of crystal structure, sample synthesis, characterization, and Rietveld refinement are given in the Supplemental Material [17] (see Figs. S1, S2, S3 and Tables I and II). A more detailed study of electronic and magnetic properties is given in [15]. Micro-Raman experiments in backscattering geometry using a 50× objective were carried out on small pieces (∼0.5 mm × 0.5 mm × 0.2 mm) taken from polycrystalline sintered pellets of Bi-doped $Sm_2Ir_2O_7$ samples using a LabRAM HR Evolution Spectrometer (HORIBA Jobin Yvon, Syncerity) and 532-nm excitation wavelength from a DPSS laser source. The laser power was kept at ∼0.3 mW for pure and lower doped samples ($x \leqslant 0.10$) and ∼1.7 mW for the higher doped samples. The temperature-dependent measurements were carried out using a Cryostation S50 Montana closed-cycle He cryostat. The recorded Raman spectra are fitted with a sum of Lorentzian line shapes using the nonlinear least-square fitting method in ORIGIN to extract phonon frequencies, linewidths, and intensities.

III. RESULTS AND DISCUSSIONS

Figure 1 shows the evolution of antiferromagnetic AIAO ordering temperature (T_N), metal-insulator transition temperature (T_{MIT}), and the temperature where resistivity takes a gradual upturn (T_{MIN}) with x. On the basis of this, the electronic properties have been separated into three regions: the Weyl phase, where low temperature ρ varies as $1/T$ (for $x \leqslant 0.02$), the QBT phase with $\rho \propto -\ln T$ (for $x \geqslant 0.05$), and a new phase at the WSM-QBT boundary with $\rho \propto -T^{1/4}$ (marked V in Fig. 1) [15]. This demonstrates the presence of a quantum critical point while continuously tuning the ground state from WSM to QBT.

A. Raman spectra at ambient condition

Group-theoretical analysis of the pyrochlore structure (space group $Fd\bar{3}m$) predicts $\Gamma_{op} = A_{1g} + E_g + 4T_{2g} + 7T_{1u}$ optical and $\Gamma_{ac} = T_{1u}$ acoustic phonon modes, out of which A_{1g}, E_g, and $4T_{2g}$ phonons are Raman active, and the T_{1u} mode is IR active [18,19]. As shown in Fig. 2(a) (bottommost panel), the Raman spectra of the undoped sample ($x = 0$) show six distinct Raman modes labeled by irreducible representations based on previous studies on pyrochlore iridates [18]. A shoulder on the high-energy side of the T^4_{2g} mode can be a second-order Raman mode [20,21]. Theoretical studies on pyrochlore iridates [18–20,22,23] have shown that the A_{1g} and E_g modes mainly involve O-Ir-O bending, the T^1_{2g} and T^2_{2g} modes are predominantly associated with Sm-O stretching, the T^3_{2g} mode due to the vibration of O′ ions surrounded by eight Sm ions, and the T^4_{2g} mode related to Ir-O stretching vibration. As the cation sites of Ir^{4+} and Sm^{3+} have a center of inversion, the Raman-active modes involve only the vibrations of oxygen atoms [24]. Out of all modes, the A_{1g} and E_g modes play a crucial role as these are directly involved in the trigonal distortion of IrO_6 octahedra through the modification of the Ir-O-Ir bond angle [23,24]. The E_g mode is about twice as broad compared to other modes, similar to $Eu_2Ir_2O_7$ [18].

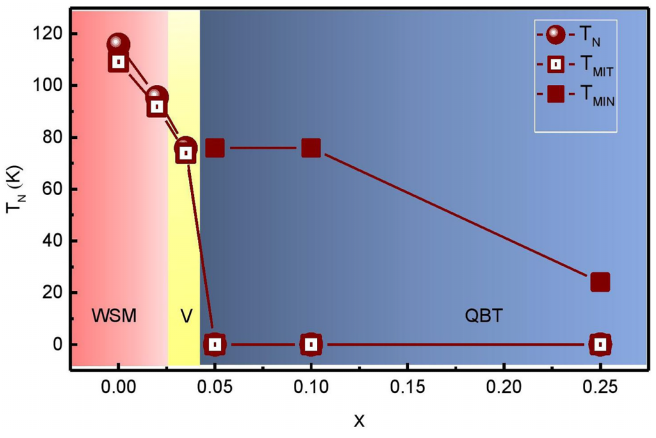

FIG. 1. The doping (x) dependence of antiferromagnetic ordering temperature (T_N), metal-to-insulator transition temperature (T_{MIT}), and the temperature where ρ shows a gradual upturn (T_{MIN}) [15].

Figure 2(a) shows the evolution of Raman spectra with Bi doping ($x = 0$, 0.02, 0.035, 0.05, 0.10, 0.25, 0.50, and 0.75). The doping dependence of different phonon modes is given in Fig. 2(b). With the increase of x, the Raman frequency of the T^4_{2g} mode decreases (∼20 cm^{-1}), but the E_g and T^2_{2g} modes shift significantly towards higher frequency (∼20 and ∼25 cm^{-1}, respectively). These trends are due to hybridization among O (2p)-Bi (6s) and Ir (5d) orbitals resulting in the modification of Sm-O and Ir-O bands [23,25,26]. For the T^1_{2g} mode, the shift is ∼6 cm^{-1}, much less as compared to the shift in other modes. Interestingly, the strong A_{1g} mode hardens by ∼8 cm^{-1} up to $x = 0.10$ of Bi doping and shows large softening by (∼42 cm^{-1}) with a further increase in x, which is consistent with the evolution of the lattice parameter with x [15]. Since the A_{1g} mode is directly involved with the O (48f) parameter [23], its modification through lattice constant affects the force constant of this vibration and causes large renormalization in its frequency. Surprisingly, the two bending modes (A_{1g} and E_g) are influenced differently by doping, which is similar to our recent studies on $Eu_2Ir_2O_7$ [27], which has been attributed to the fact that the modes are renormalized differently by electron-phonon coupling in the metallic state at room temperature.

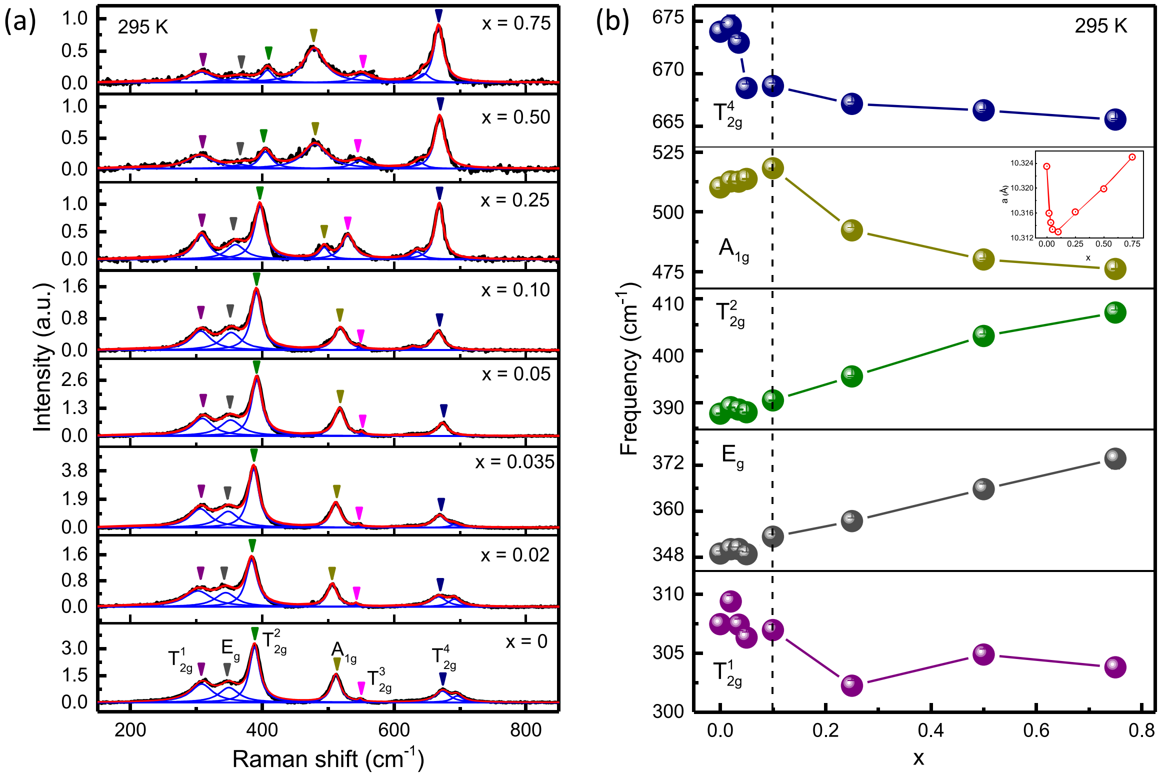

FIG. 2. (a) Ambient Raman spectra for $x = 0$, 0.02, 0.035, 0.05, 0.10, 0.025, 0.50, and 0.75 samples; the arrows mark the phonon modes; solid red and blue lines are the cumulative and individual Lorentzian fit to the phonon modes, respectively. (b) Doping dependence of different phonon modes at ambient condition; the vertical dashed line separates the anomalous lattice contraction and normal lattice expansion region at $x = 0.10$ (inset shows the evolution of lattice parameter a with doping). The error bars on phonon frequencies are smaller than the size of the symbols.

B. Temperature-dependent Raman studies

We have performed temperature-dependent Raman measurements for undoped and doped ($x \leqslant 0.10$) samples from 295 to 5 K covering the spectral range from 70 to 1760 cm^{-1}. The crystal symmetry does not change across MIT [28]. Figure 3(a) shows unpolarized Raman spectra of pure $Sm_2Ir_2O_7$ at three representative temperatures. As expected from the preservation of crystal symmetry across T_N, the number of Raman modes remains the same. For the parent sample below T_N, the phonon modes are superimposed on a broad continuum centered at ∼460 cm^{-1} (∼57 meV), as observed in Fig. 3(a). A flat electronic continuum arising from excitations of free carriers and extending at least up to 1760 cm^{-1} with linearly increased intensity at small frequencies is also observed at low

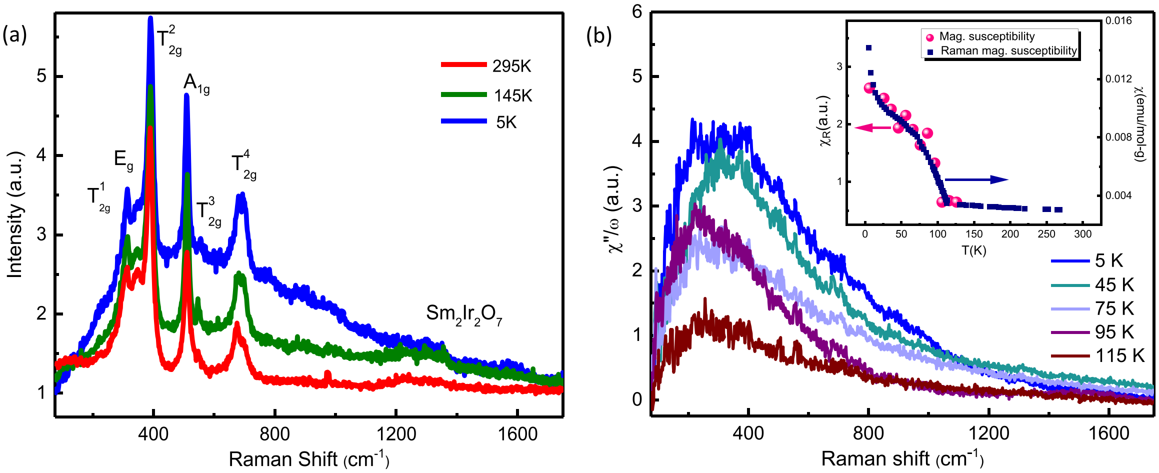

FIG. 3. (a) Temperature-dependent unpolarized Raman spectra of pure $Sm_2Ir_2O_7$ at three representative temperatures. (b) Temperature evolution of Raman conductivity derived from raw intensity. Inset: Raman magnetic susceptibility superimposed on the field cooled susceptibility curve; the arrows define the Y axis.

temperatures for the $x = 0.05$ and 0.10 samples (discussed later in Sec. III B 2).

1. Origin of broad continuum in pure $Sm_2Ir_2O_7$

We first address the broad underlying continuum observed for the $x = 0$ sample. This continuum is strongly temperature dependent. The complete disappearance of this feature above T_N indicates that its origin can be magnetic. To further understand the evolution of this broad magnetic continuum, we have evaluated the dynamic spin susceptibility associated with this continuum. Figure 3(b) shows the temperature dependence of Raman conductivity $\chi''(\omega)/\omega$ where Raman susceptibility $\chi''(\omega) = I(\omega)/[1 + n(\omega)]$. Here $I(\omega)$ is the measured Raman intensity, and $1 + n(\omega) = 1/(1 - e^{-h\omega/kT})$ is the Bose thermal factor. Here the phonon modes have been suppressed. The dynamic spin susceptibility is then obtained by integrating the Raman conductivity within the frequency range of 70–1760 cm^{-1}, $\chi_R = \lim_{\omega\to 0}\chi(k = 0, \omega) \equiv \frac{2}{\pi}\int \frac{\chi''(\omega)}{\omega} d\omega$. The inset shows the temperature evolution of χ_R, which superimposes very well with the measured field-cooled magnetic susceptibility curve [15]. We, therefore, assign the broad background below T_N as magnetic Raman scattering due to spin-spin correlations, which becomes Raman active by virtue of strong SOC and non-noncollinear long-range magnetic ordering [29]. It should be noted that the magnetic continuum is not observed in the case of doped samples, even though $x = 0.02$ and 0.035 samples show a magnetic ground state. The absence of magnetic Raman scattering in these samples may be due to smearing of the Raman signal due to nonmagnetic Bi defects or shifting of the peak position near to the cut-off range.

2. Electronic Raman scattering in doped metallic samples

We now focus on the nonmagnetic metallic samples in the crossover region and in close proximity to QBT. The presence of QBT near the Fermi energy suggests that these materials can be tuned to various topological phases [30]. Further, the quadratic nodal semimetals themselves are transformed into a non-Fermi-liquid state where electrons are dominated by long-range Coulomb interactions, and they lose coherence [31].

Keeping this in mind, we proceed to analyze the flat continuum observed in the $x = 0.05$ and 0.10 samples at low temperatures, which extends at least up to 1760 cm^{-1} [see Fig. 4(a)] (showing 5 K Raman spectra for $x = 0$, 0.02, 0.035, 0.05, and 0.10). Its absence in antiferromagnetic insulating samples (i.e., for $x \leqslant 0.035$) suggests its origin to be electronic and predominantly arising from the electronic Raman scattering (ERS) from the free carriers. The observed ERS has the strongest amplitude at the lowest measured temperature, and the amplitude decreases as temperature increases. The background becomes flat above 200 K for the $x = 0.05$ sample and above 70 K for the $x = 0.10$ sample [see Figs. S4(a) and S4(b) [17]]. This continuum is a universal feature of strongly correlated systems such as high-T_c superconductors and has been analyzed using a phenomenological model [32–36] (first brought out by Götze and Wöffle [37]) by fitting the Raman response by memory function formalism. The complex Raman response function $\chi(\omega)$ in terms of memory function $M(\omega)$ is given by [33,37,38]

$$\chi(\omega, T) = \frac{M(\omega, T)}{\hbar\omega + M(\omega, T)}, \qquad (1)$$

where $M(\omega, T) = \hbar\omega\lambda(\omega, T) + i\Gamma_s(\omega, T)$, dynamical scattering rate $\Gamma_s(\omega)$ and mass enhancement factor $\lambda(\omega)$ are related by Kramers-Kronig transformation. Thus, the imaginary part related to the Raman spectrum is

$$\chi_e''(\omega, T) = \frac{R\hbar\omega\Gamma_s(\omega, T)}{\{\hbar\omega[1 + \lambda(\omega, T)]\}^2 + [\Gamma_s(\omega, T)]^2}. \qquad (2)$$

The dynamical scattering rate $\Gamma_s(\omega)$ follows the form [38]

$$\Gamma_s(\omega, T) = [\Gamma_{\mathrm{imp}} + \sqrt{\beta^2K^2T^2 + \hbar^2\omega^2}]\phi\left(\frac{\omega}{\omega_c}\right), \qquad (3)$$

where Γ_{imp} is the static scattering rate, β determines the relative strength of the elastic and inelastic scattering processes (optimized to a value of π for all temperatures), and $\phi(\frac{\omega}{\omega_c}) = \frac{1}{1+(\frac{\omega}{\omega_c})^2}$ is the cut-off function with cut-off frequency ω_c. The parameter R in Eq. (2) represents the strength of ERS. For the study of carrier properties, a typical value of cut-off frequency is of the order of the bandwidth of charge carriers (for half-filled iridates it is ~0.4 eV). It is seen that fitting the above model with our Raman data converges with the marginal Fermi-liquid (MFL) form of Γ_s for the measured range of temperatures until the background becomes flat [see Figs. 4(b) and 4(c)]. Here, the MFL behavior arises from the breakdown of conventional Fermi-liquid behavior at low temperatures due to enhanced particle-particle interaction in the QBT state [39,40]. Figure 4(d) shows the temperature evolution of the prefactor R used while fitting the electronic continuum at various temperatures. It is noticeably clear from Fig. 4(d) that the amplitude of ERS is strongly temperature dependent and decreases continuously with increasing temperatures in the case of the $x = 0.10$ sample. For $x = 0.05$, the prefactor remains almost constant at low temperatures and shows a drastic fall near ~125 K, marked as T_Q. Since the origin of ERS in doped $\mathrm{Sm_2Ir_2O_7}$ samples is driven by the enhanced scale of interactions in the QBT state, T_Q can be the characteristic temperature above which the band structure does not have QBT, hence weakening the ERS.

3. Phonon self-energies in $Sm_2Ir_2O_7$

Now, we will proceed to understand the Sm-Bi system in terms of phonon self-energies. Figures 5(a) and 5(b) show the temperature dependence of phonon frequencies and linewidths for the A_{1g}, E_g, and three T_{2g} phonons. In general, the phonon self-energies depend on phonon-phonon, electron-phonon, and spin-phonon interactions ($\varepsilon_{pp} + \varepsilon_{ep} + \varepsilon_{sp}$). The frequency and linewidths are related to the real and imaginary parts of the phonon self-energies, respectively. In order to extract the contribution of spin-phonon coupling below T_N, we fit the temperature dependence of the phonon frequencies and linewidths above T_N with a simple cubic anharmonic model where the phonon decays into two phonons of equal frequency: $\omega(T) = \omega_0 + CG(\omega, T)$ and $\Gamma(T) = \Gamma_0 + DG(\omega, T)$ where $G(\omega, T) = [1 + 2n(\omega_0/2)]$ [41]. The parameters C and D are related to phonon-phonon interaction strength, with the parameter $C < 0$, and $D > 0$. The solid red

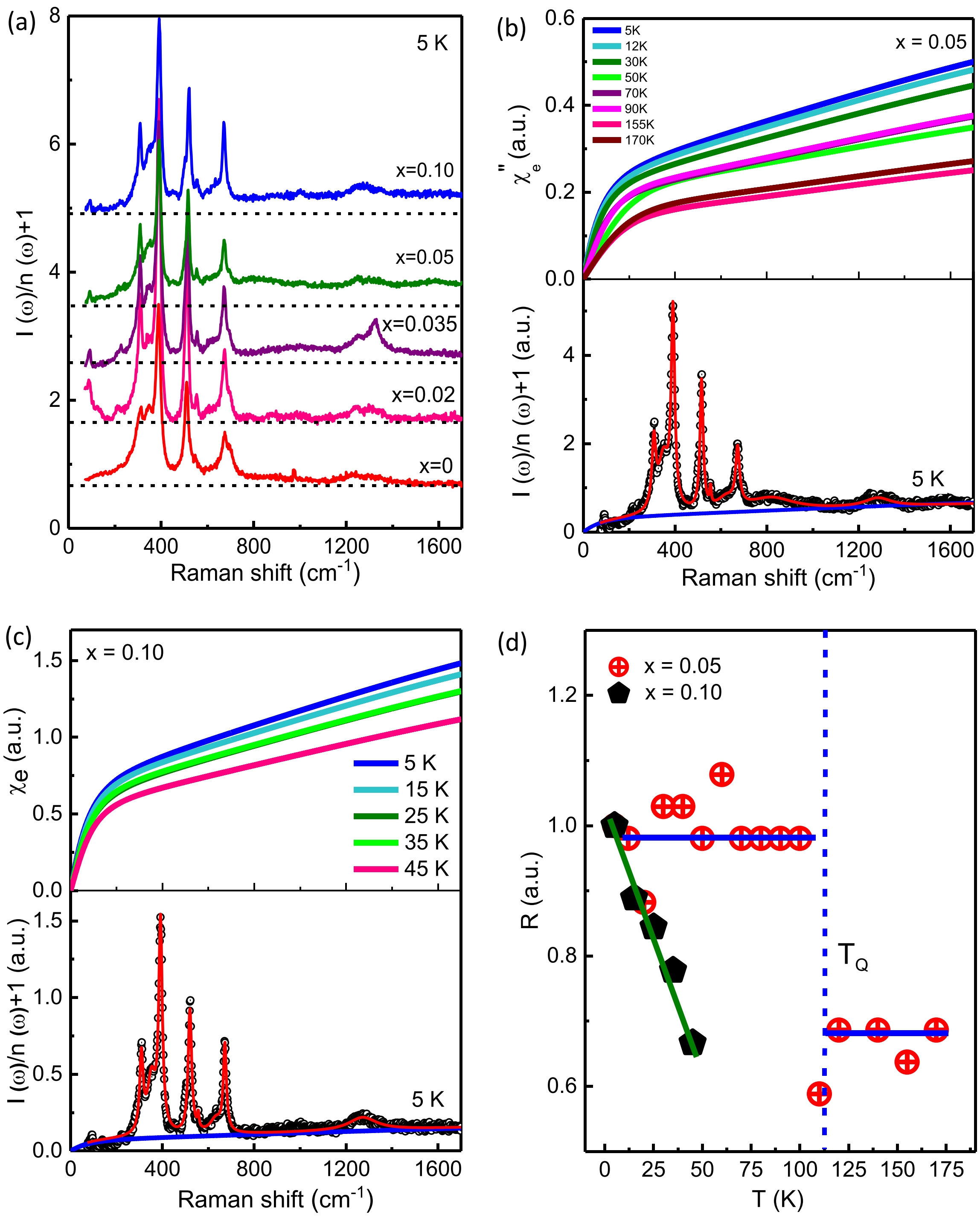

FIG. 4. (a) 5 K Raman spectra of parent and doped samples; the horizontal dashed line indicates the flat baseline of the $x = 0$ and 0.02 samples and the deviation from flat behavior due to electronic continuum present in the $x \geqslant 0.05$ samples extending at least up to 1760 cm^{-1} (the data has been shifted vertically for representation). (b) and (c) Raman spectra for $x = 0.05$ and 0.10, respectively; the bottom panels indicate data at the lowest measured temperature, i.e., 5 K; solid red lines are the cumulative Lorentzian fit to the phonon modes, and solid blue lines show the fit to the electronic continuum by the MFL model; the top panels show the fitted continuum at various measured temperatures. (d) Temperature evolution of the prefactor R of the MFL model for $x = 0.10$ and 0.05; the vertical blue dashed line indicates T_Q, and the solid blue and green lines are guides to the eye.

lines in Figs. 5(a) and 5(b) are the fits to the cubic anharmonic model, extrapolated by dotted lines below T_N.

It is very clear from Figs. 5(a) and 5(b) that all the mode frequencies and linewidths (FWHM) show significant deviation from the expected anharmonic behavior below T_N. The noteworthy observations are as follows: (i) anomalous softening of frequencies of T_{2g}^1, E_g, A_{1g}, and T_{2g}^4 modes (between T_N and 50 K), (ii) the linewidth of the T_{2g}^1 mode

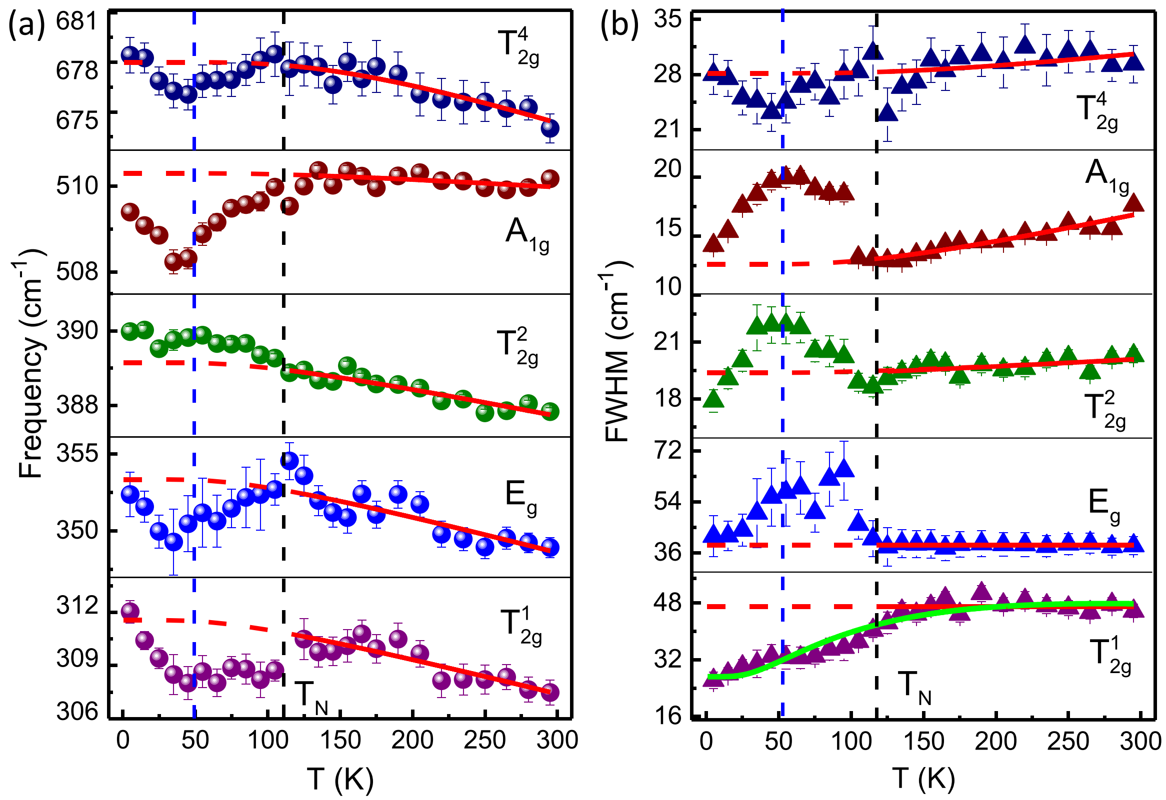

FIG. 5. (a) and (b) Temperature variation of phonon frequencies and linewidths of pure $Sm_2Ir_2O_7$; the solid red lines are fit to the anharmonic model and are extrapolated to 0 K by red dashed lines. The vertical black and blue dashed lines indicate T_N and crossover into Weyl phase, respectively. The solid green line is fit to the electron-phonon model.

showing a large decrease below T_N (by ~35 cm^{-1}), and (iii) a sudden jump in linewidth of E_g (~20 cm^{-1}) and A_{1g} (~5 cm^{-1}) near T_N. These nontrivial behaviors cannot be explained considering the monotonic temperature dependence due to the phonon-phonon interactions alone and indicate that the phonon frequencies and linewidths are renormalized by spin-phonon interactions below T_N. The substantial, large linewidth anomalies, similar to those in $Eu_2Ir_2O_7$ [18] and insulating square lattices $Sr_2Ir_2O_4$ and $Sr_3Ir_2O_7$ [42], can arise from the phonon induced modulation of the orbitals. The partial admixture of the low-lying $J_{\text{eff}} = 3/2$ excited state into the crystal field induced $J_{\text{eff}} = 1/2$ ground state in the presence of static or dynamic lattice distortions activates pseudospin-phonon coupling by low-energy shape fluctuations of the valence-electron cloud that effectively couple to phonons and can cause phonon linewidth anomalies [18,42–44]. In contrast to 3d and 4d TMOs [43,45,46], $Sm_2Ir_2O_7$ shows large frequency shifts for E_g, T^1_{2g}, and T^4_{2g} modes and exceptionally high linewidth variation in all of the modes. Similar large phonon renormalizations have been reported in $Cd_2Os_2O_7$ [47] and have been attributed to effective magnetoelastic coupling by virtue of strong SOC induced orbital contribution to the magnetism.

We now proceed to understand the phonon anomalous behavior near T_N in detail. In this context, similar anomalies are seen for the E_g mode in the Raman study of $Eu_2Ir_2O_7$ [18], for the Ir-O stretching mode in $Cd_2Os_2O_7$ [47], for the A_{1g} and Ir-O stretching modes in $Y_2(Ir_{1-x}Ru_x)_2O_7$ [48], and three infrared phonons associated with Ir-O-Ir bending modes in $Y_2Ir_2O_7$ [49]. These anomalies below T_N have been attributed to strong spin-phonon coupling arising from the interaction between lattice and magnetic degrees of freedom in an AIAO magnetically ordered state. Spin-phonon coupling is caused by the modulation of spin-exchange parameters by the atomic displacements in different vibrational modes. In $Cd_2Os_2O_7$, the spin-phonon coupling is known to be mediated by single-ion anisotropy interaction [50], whereas in 3d and 4d TMOs, modulation of isotropic exchange interaction originates spin-phonon coupling [43,45,46,51–54]. The SOC induced $J_{\text{eff}} = 1/2$ ground state of pyrochlore iridates makes the single-ion anisotropy term negligible in the spin Hamiltonian [55], and the phonon renormalization in these compounds cannot be explained by isotropic exchange interaction alone as the noncollinear magnetic ordering is mainly induced by SOC dominant Dzyaloshinskii-Moriya interaction. Hence, for pyrochlore iridates, the spin Hamiltonian mainly involves two leading terms and has the form [8,49]

$$H_{\text{spin}} = \sum_{ij}^{\text{NN}} J_{ij}(S_i, S_j) + \sum_{ij}^{\text{NN}} D_{ij}(S_i \times S_j), \tag{4}$$

where J_{ij} and D_{ij} are the coefficient of the isotropic exchange interaction and Dzyaloshinskii-Moriya interaction, respectively, between the i^{th} and j^{th} pseudospins of the Ir ion denoted by S_i and S_j (NN refers to the nearest-neighbor interaction). As the phonon renormalization in the pyrochlore iridates is mainly attributed to the change in Ir-O-Ir bond angle (θ) and Ir-O bond length (l), the phonon frequency shift can be written as [49,50,56]

$$\Delta\omega \sim \frac{-2}{I_m\omega}\left(\sum_{ij}^{\mathrm{NN}}\frac{\partial^2 J_{ij}(\theta,l)}{\partial p^2}\langle S_i S_j\rangle + \sum_{ij}^{\mathrm{NN}}\frac{\partial^2 D_{ij}(\theta,l)}{\partial p^2}\langle S_i \times S_j\rangle\right), \tag{5}$$

where I_m is the rotational moment of inertia and p can be θ or l depending on the phonon mode.

Here we focus on the Ir-O-Ir bending (A_{1g} and E_g) and the Ir-O stretching (T_{2g}^4) modes, which are of importance in pyrochlore iridates. All three modes reveal frequency and linewidth anomalies near T_N in $Sm_2Ir_2O_7$. The anomalous frequency softening below T_N is predominantly driven by the negative sign of $\frac{\partial^2 D_{ij}(\theta,l)}{\partial p^2}$. In this context, the phonon renormalization for bending modes is attributed to the modulation of the Dzyaloshinskii-Moriya interaction as in $Y_2Ir_2O_7$ and $Eu_2Ir_2O_7$ [18,49], whereas the renormalization of the stretching mode can be attributed to the modulation of the isotropic exchange interaction as in conventional spin-phonon coupling [45,57,58]. The change in bond length of Ir-O can affect the orbital overlap integral, resulting in significant modification of J_{ij} and consequently results in phonon frequency renormalization [59]. The strength of the spin-phonon coupling will vary depending on the dynamic modulation of D_{ij} and J_{ij} by lattice vibrations. Hence, phonon renormalization is different for different phonon modes, as evident from Fig. 5. Both E_g and A_{1g} modes are mostly affected by spin-phonon coupling and show drastic changes below T_N. The frequency renormalization by spin-phonon coupling is also noticeable in other phonons, T_{2g}^1 and T_{2g}^4, whereas the T_{2g}^2 frequency (Sm-O stretching) remains unaffected by spin-phonon coupling.

The observed minima in frequencies and maxima in linewidths at ~50 K suggest that there are at least two competitive interactions. As earlier predicted by theory [4,6,7] and recent transport measurements by Telang *et al.*, the WSM state in $Sm_2Ir_2O_7$ is established at temperatures lower than T_N. In other words, the band structure continues to evolve below T_N and stabilizes the WSM state as its ground state at lower temperatures where contributions from thermal or other mechanisms do not dominate. In WSM, since the Weyl points lie in close proximity to the Fermi energy (E_f), the interband electronic transitions across the nodes can be significantly affected by thermal excitations of the carriers and occurs in a low-energy range of 2μ (μ is the chemical potential with respect to the Weyl points) [60,61]. This energy scale overlaps that of optical phonons and modulates the phonon self-energy that is coupled to these transitions. Thus, the anomaly at ~50 K is likely to be due to the topological phase transition into the WSM state. Note that in our Raman data, this renormalization can be seen only for the $x = 0$ and 0.02 samples (at ~50 and ~40 K, respectively) and absent for the $x = 0.035$ sample (see Fig. 6), inferring its origin associated with the formation of Weyl cones. The competition among electron-phonon, spin-phonon, and phonon-phonon interactions can result in the observed nonmonotonicity in frequencies and linewidths as a function of temperature.

Next, we discuss the large change in the linewidth of the T_{2g}^1 phonon below T_N, which is distinct from other phonons that are renormalized by spin-phonon coupling. The lattice anharmonicity is a weak effect, as can be seen by a very small change in the linewidth at $T > T_N$. As the linewidth contains information related to decay channels available to the phonon modes, we consider this temperature dependence as the zone-center optical phonon assisted creation of electron-hole pairs via interband transitions near the Fermi surface. The decay rate depends on the difference in occupation numbers of electron and hole states and follows the functional form [62,63]

$$\Gamma_{\text{el-ph}}(T) = \Gamma_0 + A[n_F(\hbar\omega_a, T) - n_F(\hbar\omega_a + \hbar\omega_{\text{ph}}, T)], \tag{6}$$

where $\hbar\omega_{\text{ph}}$ is the energy of the optical phonon, n_F is the Fermi-Dirac occupation factor, and $\hbar\omega_a$ denotes the distance between E_F and the initial state of the electron. Γ_0 is the temperature-independent term originating from the scattering of phonons by defects, and A is the fitting parameter related to the electron-phonon interaction strength. The fitted curve (green color) in the lowest panel of Fig. 5(b) shows that this model agrees very well with our experimental data over the entire temperature range. The observation that it is only significant in the case of the T_{2g}^1 phonon can be rationalized based on the fact that the electron-phonon coupling strength depends on the symmetry and energy of the optical phonon. The doped samples are discussed in more detail in the next section.

4. *Effect of doping*

With temperature variation, the crystal symmetry does not change, and the same number of phonons are observed for doped samples. However, one weak additional mode, marked N_1, is observed at low temperatures below T_N near ~86 cm^{-1} (see Figs. S5, S6, S7, and S8) [17]. As this low-frequency mode is also seen for the doped samples, including $x = 0.05$ and 0.10 that do not show a magnetic transition [15], we suggest that it can be due to the lowering of crystal symmetry at some crystallographic sites, thus making infrared-active modes also Raman active, similar to $Cd_2Os_2O_7$ showing a zone-center infrared (IR) phonon near ~85 cm^{-1} below T_N [64]. To quantify the temperature dependence of modes, following the same approach as for the pure sample, the phonon frequencies and linewidths of doped samples are fitted with the cubic anharmonic model at higher temperatures (above T_N for the $x = 0.02$ and 0.035 and above T_Q for the $x = 0.05$ and 0.10 samples), and the fitted curves are extrapolated to 0 K, as shown in Figs. 6(a)–6(d) and Figs. 7(a)–7(d).

(a) Phonon anomalies for doped systems ($x = 0.02$ and 0.035) showing magnetic transition. For $x = 0.02$ and 0.035, T_N falls to ~90 and ~60 K, respectively. In terms of phonons, all mode frequencies deviate from the anharmonic phonon-phonon interaction model below T_N (see Fig. 6). For $x = 0.02$, the phonons exhibit an abnormal frequency softening between T_N and ~40 K, similar to the $x = 0$ case, which we attributed to a transition to WSM state. The T_{2g}^2 frequency (Sm-O vibrations) has a nonmonotonic dependence on temperature for

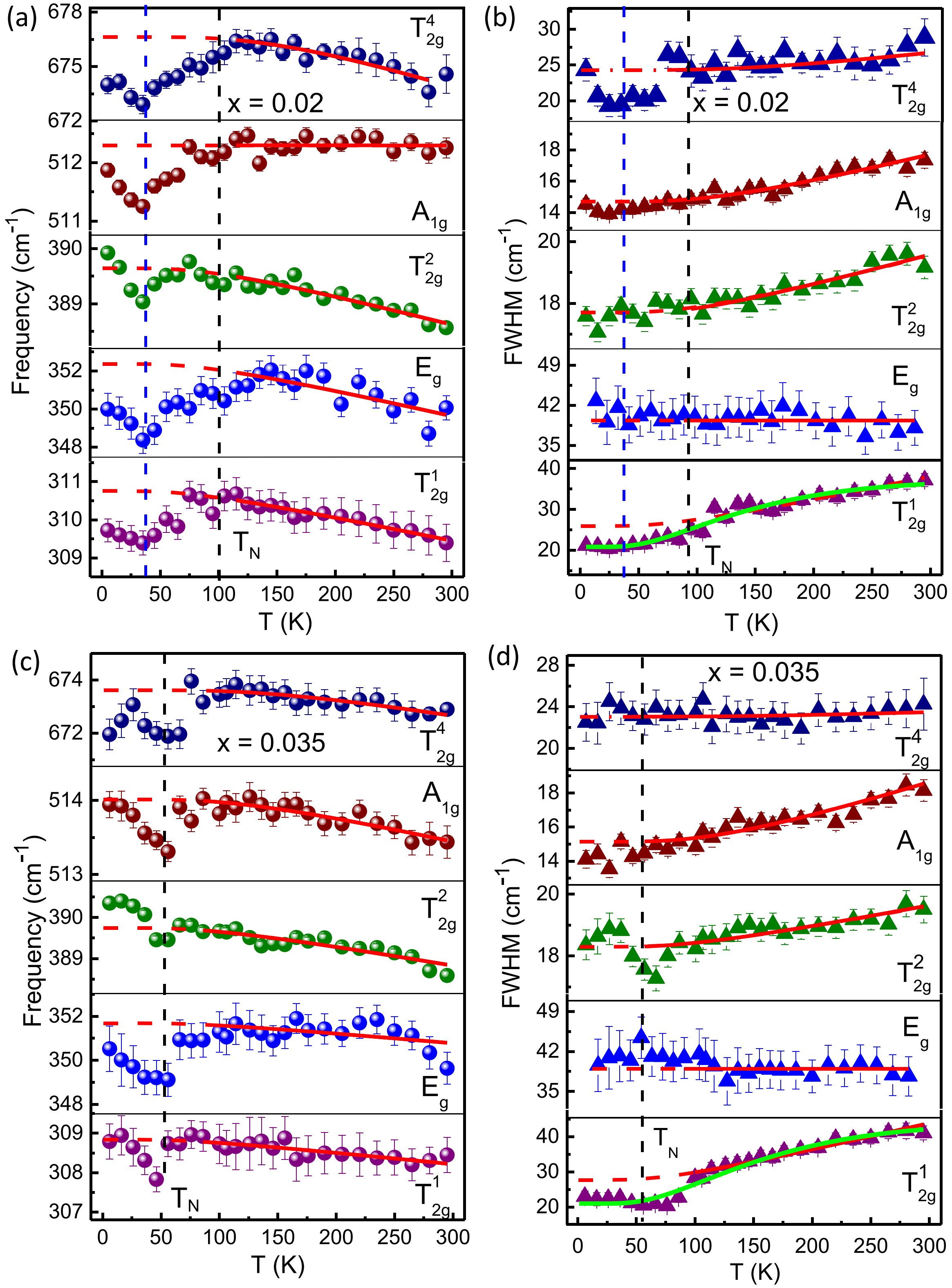

FIG. 6. (a)–(d) Temperature evolution of phonon frequencies and linewidths for the $x = 0.02$ [(a) and (b)] and 0.035 [(c) and (d)] samples, respectively. The vertical dashed lines and the solid red and green lines have the same meaning as Fig. 5.

$x = 0.02$, which was not seen in the pure sample. This suggests that the Sm-O$_6$-O$'_2$ scalenohedron of the pyrochlore unit cell has undergone some rearrangements with the replacement of Bi ions. In comparison to the $x = 0$ sample, the linewidth of all modes decreases with temperature. We note that, for the T^1_{2g} phonon, the decrease in linewidth with temperature is very large as compared to other modes, suggesting an additional mechanism to anharmonic interactions. We have fitted the data

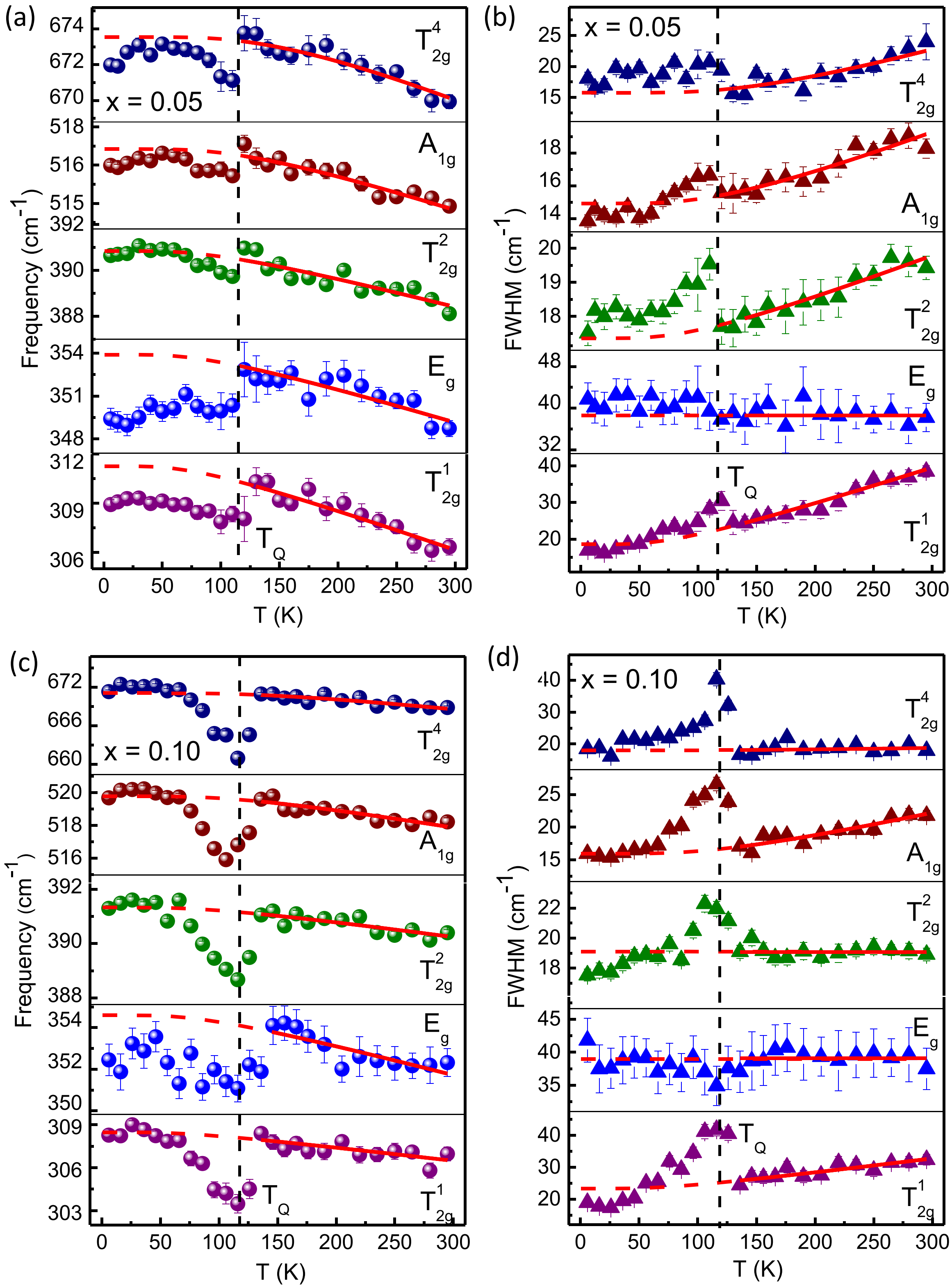

FIG. 7. (a)–(d) Temperature evolution of phonon frequencies and linewidths for $x = 0.05$ [(a) and (b)] and 0.10 [(c) and (d)] samples, respectively; the vertical dashed lines indicate T_Q; the solid red lines have the same meaning as Fig. 5.

with Eq. (6) representing the electron-phonon coupling, the dominant source of broadening. It is evident from Fig. 6 that the magnitude of renormalization decreases with Bi doping, suggesting that the tuning of bandwidth and magnetic ordering with Bi substitution weakens the spin-phonon interaction.

(b) Phonon anomalies for doped metallic samples ($x = 0.05$ and 0.10). While transport and susceptibility measurements show metallic behavior and no magnetic ordering down to 2 K for $x = 0.05$ and 0.10, it is interesting to note that the Raman modes exhibit considerable temperature-dependent anomalies

at ~125 K, denoted as T_Q in Fig. 7. In particular, for $x = 0.05$, the frequencies of all phonons, as well as the linewidths of the three T_{2g} and A_{1g} phonons, differ from the anharrmonic model and show discontinuities around T_Q. At $x = 0.10$, the magnitude of phonon anomalies (deviation from the anharmonic model) is even larger. The linewidths exhibit a sharp rise at T_Q (by ~10 cm^{-1} for T_{2g}^1, T_{2g}^4, and A_{1g} and by ~2 cm^{-1} for T_{2g}^2) followed by a decrease with lowering of the temperature. This anomalous behavior is not seen for the linewidth of the E_g mode. It is clearly evident from Figs. 6 and 7 that the anomalous behavior for the nonmagnetic systems ($x = 0.05$ and 0.10), is very different for systems showing antiferromagnetic transition with varying T_N, indicating a different origin of phonon renormalization.

We note that the samples with $x = 0.05$ and 0.10 (Fig. 1) though metallic show an upturn in resistivity at low temperatures [15] indicating a nontrivial ground state. Similar resistivity upturn has been previously observed upon cooling in a three-dimensional (3D) Luttinger semimetal $Pr_2Ir_2O_7$ and attributed to crossover into QBT state [65]. The resistivity of $Pr_2Ir_2O_7$ shows a minimum at low temperatures below which the resistivity shows a $-\ln T$ increase but with no signs of magnetic ordering or freezing. This minimum is a consequence of the interplay between the temperature dependence of an interaction between a lowering scattering rate and a decreasing charge density upon cooling in the 3D QBT state. Because the threshold to excite thermal carriers is low, unlike conventional metals, the charge density in such a system can be strongly temperature dependent over a wide temperature range. The competition between temperature dependencies between plasma frequency and scattering rates can effectively result in the observed dip in dc resistivity. The appearance of resistivity minimum at a low temperature with a $-\ln T$ behavior (upon cooling) without any magnetic ordering, therefore, appears to be a common feature of these pyrochlores in close proximity of the QBT. The electron-electron interaction in these materials is predicted to be more pronounced than linear band-crossing systems due to the enhanced electronic density of states [31,65]. Further, the enhanced low-energy phonon-assisted electronic excitations near the band touching points will result in strong electron-phonon coupling, contributing significantly to the phonon self-energies and hence resulting in phonon anomalies, very different from the spin-phonon coupling or lattice anharmonicity.

Additionally, we examined the sample with $x = 0.25$'s temperature-dependent phonon behavior (see Fig. S9 [17]) to validate the origin of the electron-phonon coupling in samples with $x = 0.05$ and 0.10. It is evident from Figs. S9(b) and S9(c) that the phonon frequencies and linewidths are monotonic and clearly follow the anharmonic trend, inferring absence of electron-phonon interaction. The absence of such scattering could be explained based on the transport behavior of these samples. It is clearly apparent from the resistivity curve [Fig. S10 (a) [17]] that the $x = 0.25$ sample lies more towards the metallic regime with orders of magnitude decrease in the resistivity. Although the low-temperature resistivity upturn is still there [inset of Fig. S10 (a)], it is weak compared to the $x = 0.05$ and 0.10 samples. Figures S10(b) and S10(c) [17] show the comparison of various scaling behaviors of resistivity for $x = 0.25$. Evidently, the linear behavior can be seen in both panels (b) and (c). However, the linearity is more pronounced in the case of a variable range hopping model, which is a characteristic of the disordered systems, suggesting that the $-\ln T$ dependence (QBT) is becoming increasingly suppressed with further Bi doping. Hence, it is reasonable to conclude that the QBT is becoming increasingly suppressed in the presence of increasing Bi disorder, which also validates the absence of electron-phonon coupling for $x = 0.25$. We hope that our experimental results will motivate a quantitative understanding of phonon self-energies in 3D QBT systems.

IV. CONCLUSION

In summary, we observe strong phonon renormalization in pure and doped samples $(Sm_{1-x}Bi_x)_2Ir_2O_7$ ($x = 0$, 0.02, and 0.035) below T_N due to strong spin-phonon coupling. Our Raman results on the pure $Sm_2Ir_2O_7$ showed evidence of pronounced dynamic spin-spin correlations in the AIAO-ordered state. The temperature-dependent Raman spectra of pure and doped samples exclude the presence of any structural transition across the MIT. Phonon anomalies at a much lower temperature (> 50 K) than T_N are observed and provide qualitative support to the existence of WSM state in the $x = 0$ and 0.02 samples. The QBT candidates ($x = 0.05$ and 0.10) show strong signatures of ERS, analyzed using Raman susceptibility for the non-Fermi-liquid state. These systems also show strong phonon anomalies driven by the enhanced electron-phonon interaction in the QBT state. Our results support the possibility of exotic topological states near the metal-insulator boundary, further motivating the search for more theoretical and experimental evidence in these systems, along with a quantitative understanding of phonon renormalization.

ACKNOWLEDGMENTS

A.K.S. thanks the Department of Science and Technology, Government of India for financial support under the National Science Chair Professorship and the Nanomission. M.R. would like to thank the Micro Nano Characterization facility (MNCF) at Center for Nanoscience and Engineering (CeNSE), IISc for material characterization.

---

[1] C. Donnerer, M. C. Rahn, M. M. Sala, J. G. Vale, D. Pincini, J. Strempfer, M. Krisch, D. Prabhakaran, A. T. Boothroyd, and D. F. McMorrow, All-in–all-Out Magnetic Order and Propagating Spin Waves in $Sm_2Ir_2O_7$, Phys. Rev. Lett. **117**, 037201 (2016).

[2] Y. Wang, T. F. Rosenbaum, D. Prabhakaran, A. T. Boothroyd, and Y. Feng, Approaching the quantum critical point in a highly correlated all-in–all-out antiferromagnet, Phys. Rev. B **101**, 220404(R) (2020).

[3] L. Savary, E.-G. Moon, and L. Balents, New Type of Quantum Criticality in the Pyrochlore Iridates, Phys. Rev. X **4**, 041027 (2014).

[4] X. Wan, A. M. Turner, A. Vishwanath, and S. Y. Savrasov, Topological semimetal and Fermi-arc surface states in the

electronic structure of pyrochlore iridates, Phys. Rev. B **83**, 205101 (2011).

[5] K.-H. Ahn, K.-W. Lee, and W. E. Pickett, Spin-orbit interaction driven collective electron-hole excitations in a noncentrosymmetric nodal loop Weyl semimetal, Phys. Rev. B **92**, 115149 (2015).

[6] W. Witczak-Krempa and Y. B. Kim, Topological and magnetic phases of interacting electrons in the pyrochlore iridates, Phys. Rev. B **85**, 045124 (2012).

[7] M. Kargarian, J. Wen, and G. A. Fiete, Competing exotic topological insulator phases in transition-metal oxides on the pyrochlore lattice with distortion, Phys. Rev. B **83**, 165112 (2011).

[8] R. Yadav, M. Pereiro, N. A. Bogdanov, S. Nishimoto, A. Bergman, O. Eriksson, J. van den Brink, and L. Hozoi, Heavy-mass magnetic modes in pyrochlore iridates due to dominant Dzyaloshinskii-Moriya interaction, Phys. Rev. Mater. **2**, 074408 (2018).

[9] S. Nakatsuji, Y. Machida, Y. Maeno, T. Tayama, T. Sakakibara, J. van Duijn, L. Balicas, J. N. Millican, R. T. Macaluso, and J. Y. Chan, Metallic Spin-Liquid Behavior of the Geometrically Frustrated Kondo Lattice $Pr_2Ir_2O_7$, Phys. Rev. Lett. **96**, 087204 (2006).

[10] H. Zhang, K. Haule, and D. Vanderbilt, Metal-Insulator Transition and Topological Properties of Pyrochlore Iridates, Phys. Rev. Lett. **118**, 026404 (2017).

[11] K. Matsuhira, M. Wakeshima, R. Nakanishi, T. Yamada, A. Nakamura, W. Kawano, S. Takagi, and Y. Hinatsu, Metal-insulator transition in pyrochlore iridates $Ln_2Ir_2O_7$ (Ln = Nd, Sm, and Eu), J. Phys. Soc. Jpn. **76**, 043706 (2007).

[12] K. Matsuhira, M. Wakeshima, Y. Hinatsu, and S. Takagi, Metal–insulator transitions in pyrochlore oxides $Ln_2Ir_2O_7$, J. Phys. Soc. Jpn. **80**, 094701 (2011).

[13] S. M. Disseler, C. Dhital, A. Amato, S. R. Giblin, C. de la Cruz, S. D. Wilson, and M. J. Graf, Magnetic order in the pyrochlore iridates $A_2Ir_2O_7$ (A = Y, Yb), Phys. Rev. B **86**, 014428 (2012).

[14] M. Graf, S. Disseler, C. Dhital, T. Hogan, M. Bojko, A. Amato, H. Luetkens, C. Baines, D. Margineda, S. Giblin, M. Jura, and S. Wilson, Magnetism and magnetic order in the pyrochlore iridates in the insulator-to-metal crossover region, J. Phys.: Conf. Ser. **551**, 012020 (2014).

[15] P. Telang and S. Singh, Protracting the Weyl phase by a giant negative lattice expansion in Bi doped $Sm_2Ir_2O_7$, arXiv:2106.03512.

[16] P. Hosur, S. A. Parameswaran, and A. Vishwanath, Charge Transport in Weyl Semimetals, Phys. Rev. Lett. **108**, 046602 (2012).

[17] See Supplemental Material at http://link.aps.org/supplemental/10.1103/PhysRevB.108.035133 for information on the crystal structure, sample synthesis, and Rietveld refinement (Figs. S1–S3, Tables I and II). The ERS (observed in doped samples) is suppressed at higher temperatures, as shown in Fig. S4, and the temperature evolution of the Raman spectra for $x = 0.02, 0.035, 0.05$, and 0.10 is displayed in Figs. S5–S8. The absence of QBT and electron-phonon coupling in the $x = 0.025$ sample is shown in Figs. S9 and S10.

[18] K. Ueda, R. Kaneko, A. Subedi, M. Minola, B. J. Kim, J. Fujioka, Y. Tokura, and B. Keimer, Phonon anomalies in pyrochlore iridates studied by Raman spectroscopy, Phys. Rev. B **100**, 115157 (2019).

[19] T. Hasegawa, N. Ogita, K. Matsuhira, S. Takagi, M. Wakeshima, Y. Hinatsu, and M. Udagawa, Raman scattering study in iridium pyrochlore oxides, J. Phys.: Conf. Ser. **200**, 012054 (2010).

[20] M. L. Sanjuán, C. Guglieri, S. Díaz-Moreno, G. Aquilanti, A. F. Fuentes, L. Olivi, and J. Chaboy, Raman and x-ray absorption spectroscopy study of the phase evolution induced by mechanical milling and thermal treatments in $R_2Ti_2O_7$ pyrochlores, Phys. Rev. B **84**, 104207 (2011).

[21] C. L. Tracy, J. Shamblin, S. Park, F. Zhang, C. Trautmann, M. Lang, and R. C. Ewing, Role of composition, bond covalency, and short-range order in the disordering of stannate pyrochlores by swift heavy ion irradiation, Phys. Rev. B **94**, 064102 (2016).

[22] H. Han, L. Zhang, H. Liu, L. Ling, W. Tong, Y. Zou, M. Ge, J. Fan, C. Zhang, L. Pi, and Y. Zhang, Electron paramagnetic resonance study of the f-d interaction in pyrochlore iridate $Gd_2Ir_2O_7$, Philos. Mag. **95**, 3014 (2015).

[23] H. Kumar and A. K. Pramanik, Nonmagnetic substitution in pyrochlore iridate $Y_2(Ir_{1-x}Ti_x)_2O_7$: Structure, magnetism, and electronic properties, J. Phys. Chem. C **123**, 13036 (2019).

[24] K. Taniguchi, T. Katsufuji, S. Iguchi, Y. Taguchi, H. Takagi, and Y. Tokura, Raman study of the metal-insulator transition in pyrochlore Mo oxides, Phys. Rev. B **70**, 100401(R) (2004).

[25] D. Liang, H. Liu, N. Liu, L. Ling, Y. Han, L. Zhang, and C. Zhang, Structural, magnetic and electrical properties in the pyrochlore oxide $Bi_{2-x}Ca_xIr_2O_{7-\delta}$, Ceram. Int. **42**, 4562 (2015).

[26] S. Brown, H. C. Gupta, J. A. Alonso, and M. J. Martínez-Lope, Lattice dynamical study of optical modes in $Tl_2Mn_2O_7$ and $In_2Mn_2O_7$ pyrochlores, Phys. Rev. B **69**, 054434 (2004).

[27] A. Thomas, P. Telang, K. Mishra, M. Cesnek, J. Bednarcik, D. V. S. Muthu, S. Singh, and A. K. Sood, Role of spin-phonon and electron-phonon interactions in the phonon renormalization of $(Eu_{1-x}Bi_x)_2Ir_2O_7$ across the metal-insulator phase transition: Temperature-dependent Raman and x-ray studies, Phys. Rev. B **105**, 075145 (2022).

[28] H. Takatsu, K. Watanabe, K. Goto, and H. Kadowaki, Comparative studies of low temperature x-ray diffraction experiments on $R_2Ir_2O_7$ (R = Nd, Eu, and Pr), Phys. Rev. B **90**, 235110 (2014).

[29] B. Singh, M. Vogl, S. Wurmehl, S. Aswartham, B. Büchner, and P. Kumar, Kitaev magnetism and fractionalized excitations in double perovskite Sm_2ZnIrO_6, Phys. Rev. Res. **2**, 013040 (2020).

[30] E.-G. Moon, C. Xu, Y. B. Kim, and L. Balents, Non-Fermi-Liquid and Topological States with Strong Spin-Orbit Coupling, Phys. Rev. Lett. **111**, 206401 (2013).

[31] T. Kondo, M. Nakayama, R. Chen, J. J. Ishikawa, E.-G. Moon, T. Yamamoto, Y. Ota, W. Malaeb, H. Kanai, Y. Nakashima, Y. Ishida, R. Yoshida, H. Yamamoto, M. Matsunami, S. Kimura, N. Inami, K. Ono, H. Kumigashira, S. Nakatsuji, L. Balents, and S. Shin, Quadratic Fermi node in a 3D strongly correlated semimetal, Nat. Commun. **6**, 10042 (2015).

[32] U. Nagel, T. Uleksin, T. Rõõm, R. P. S. M. Lobo, P. Lejay, C. C. Homes, J. S. Hall, A. W. Kinross, S. K. Purdy, T. Munsie, T. J. Williams, G. M. Luke, and T. Timusk, Optical spectroscopy shows that the normal state of URu_2Si_2 is an anomalous Fermi liquid, Proc. Natl. Acad. Sci. USA **109**, 19161 (2012).

[33] M. Opel, R. Nemetschek, C. Hoffmann, R. Philipp, P. F. Müller, R. Hackl, I. Tüttő, A. Erb, B. Revaz, E. Walker, H. Berger, and L. Forró, Carrier relaxation, pseudogap, and superconducting

gap in high-T_c cuprates: A Raman scattering study, Phys. Rev. B **61**, 9752 (2000).

[34] D. Stricker, J. Mravlje, C. Berthod, R. Fittipaldi, A. Vecchione, A. Georges, and D. van der Marel, Optical Response of Sr_2RuO_4 Reveals Universal Fermi-Liquid Scaling and Quasiparticles Beyond Landau Theory, Phys. Rev. Lett. **113**, 087404 (2014).

[35] X. K. Chen, E. Altendorf, J. C. Irwin, R. Liang, and W. N. Hardy, Oxygen-concentration dependence of the Raman continua in $YBa_2Cu_3O_y$ single crystals, Phys. Rev. B **48**, 10530 (1993).

[36] F. Kretzschmar, T. Böhm, U. Karahasanović, B. Muschler, A. Baum, D. Jost, J. Schmalian, S. Caprara, M. Grilli, C. di Castro, J. G. Analytis, J. H. Chu, I. R. Fisher, and R. Hackl, Critical spin fluctuations and the origin of nematic order in $Ba(Fe_{1-x}Co_x)_2As_2$, Nat. Phys. **12**, 560 (2016).

[37] W. Götze and P. Wölfle, Homogeneous dynamical conductivity of simple metals, Phys. Rev. B **6**, 1226 (1972).

[38] K. Sen, D. Fuchs, R. Heid, K. Kleindienst, K. Wolff, J. Schmalian, and M. Le Tacon, Strange semimetal dynamics in $SrIrO_3$, Nat. Commun. **11**, 4270 (2020).

[39] C. M. Varma, P. B. Littlewood, S. Schmitt-Rink, E. Abrahams, and A. E. Ruckenstein, Phenomenology of the Normal State of Cu-O High-Temperature Superconductors, Phys. Rev. Lett. **63**, 1996 (1989).

[40] A. Virosztek and J. Ruvalds, Raman spectrum of superconducting oxides, Phys. Rev. B **45**, 347 (1992).

[41] P. G. Klemens, Anharmonic decay of optical phonons, Phys. Rev. **148**, 845 (1966).

[42] H. Gretarsson, N. H. Sung, M. Höppner, B. J. Kim, B. Keimer, and M. Le Tacon, Two-Magnon Raman Scattering and Pseudospin-Lattice Interactions in Sr_2IrO_4 and $Sr_3Ir_2O_7$, Phys. Rev. Lett. **116**, 136401 (2016).

[43] C. Kant, J. Deisenhofer, T. Rudolf, F. Mayr, F. Schrettle, A. Loidl, V. Gnezdilov, D. Wulferding, P. Lemmens, and V. Tsurkan, Optical phonons, spin correlations, and spin-phonon coupling in the frustrated pyrochlore magnets $CdCr_2O_4$ and $ZnCr_2O_4$, Phys. Rev. B **80**, 214417 (2009).

[44] H. Gretarsson, J. Sauceda, N. H. Sung, M. Höppner, M. Minola, B. J. Kim, B. Keimer, and M. Le Tacon, Raman scattering study of vibrational and magnetic excitations in $Sr_{2-x}La_xIrO_4$, Phys. Rev. B **96**, 115138 (2017).

[45] J. S. Lee, T. W. Noh, J. S. Bae, I.-S. Yang, T. Takeda, and R. Kanno, Strong spin-phonon coupling in the geometrically frustrated pyrochlore $Y_2Ru_2O_7$, Phys. Rev. B **69**, 214428 (2004).

[46] J. Laverdière, S. Jandl, A. A. Mukhin, V. Y. Ivanov, V. G. Ivanov, and M. N. Iliev, Spin-phonon coupling in orthorhombic $RMnO_3(R = \text{Pr, Nd, Sm, Eu, Gd, Tb, Dy, Ho, Y})$: A Raman study, Phys. Rev. B **73**, 214301 (2006).

[47] T. M. H. Nguyen, L. J. Sandilands, C. H. Sohn, C. H. Kim, A. L. Wysocki, I.-S. Yang, S. J. Moon, J.-H. Ko, J. Yamaura, Z. Hiroi, and T. W. Noh, Two-magnon scattering in the 5*d* all-in-all-out pyrochlore magnet $Cd_2Os_2O_7$, Nat. Commun. **8**, 251 (2017).

[48] H. Kumar, V. G. Sathe, and A. K. Pramanik, Spin-phonon coupling in hole-doped pyrochlore iridates $Y_2(Ir_{1-x}Ru_x)_2O_7$: A Raman scattering study, J. Magn. Magn. Mater. **478**, 148 (2019).

[49] J. Son, B. C. Park, C. H. Kim, H. Cho, S. Y. Kim, L. J. Sandilands, C. Sohn, J.-G. Park, S. J. Moon, and T. W. Noh, Unconventional spin-phonon coupling via the Dzyaloshinskii–Moriya interaction, npj Quantum Mater. **4**, 17 (2019).

[50] C. H. Sohn, C. H. Kim, L. J. Sandilands, N. T. M. Hien, S. Y. Kim, H. J. Park, K. W. Kim, S. J. Moon, J. Yamaura, Z. Hiroi, and T. W. Noh, Strong Spin-Phonon Coupling Mediated by Single Ion Anisotropy in the All-In–All-Out Pyrochlore Magnet $Cd_2Os_2O_7$, Phys. Rev. Lett. **118**, 117201 (2017).

[51] S. Issing, A. Pimenov, V. Y. Ivanov, A. A. Mukhin, and J. Geurts, Composition-dependent spin-phonon coupling in mixed crystals of the multiferroic manganite $Eu_{1-x}Y_xMnO_3(0 \leqslant x \leqslant 0.5)$ studied by Raman spectroscopy, Phys. Rev. B **81**, 024304 (2010).

[52] D. A. Mota, Y. R. Barcelay, P. B. Tavares, M. R. Chaves, A. Almeida, J. Oliveira, W. S. Ferreira, and J. A. Moreira, Competing exchanges and spin–phonon coupling in $Eu_{1-x}R_xMnO_3$ (R = Y, Lu), J. Phys.: Condens. Matter **25**, 235602 (2013).

[53] S. Petit, F. Moussa, M. Hennion, S. Pailhès, L. Pinsard-Gaudart, and A. Ivanov, Spin Phonon Coupling in Hexagonal Multiferroic $YMnO_3$, Phys. Rev. Lett. **99**, 266604 (2007).

[54] H. Sakai, J. Fujioka, T. Fukuda, M. S. Bahramy, D. Okuyama, R. Arita, T. Arima, A. Q. R. Baron, Y. Taguchi, and Y. Tokura, Soft phonon mode coupled with antiferromagnetic order in incipient-ferroelectric Mott insulators $Sr_{1-x}Ba_xMnO_3$, Phys. Rev. B **86**, 104407 (2012).

[55] H. Shinaoka, T. Miyake, and S. Ishibashi, Noncollinear Magnetism and Spin-Orbit Coupling in 5*d* Pyrochlore Oxide $Cd_2Os_2\mathbf{O}_7$, Phys. Rev. Lett. **108**, 247204 (2012).

[56] E. Granado, A. García, J. A. Sanjurjo, C. Rettori, I. Torriani, F. Prado, R. D. Sánchez, A. Caneiro, and S. B. Oseroff, Magnetic ordering effects in the Raman spectra of $La_{1-x}Mn_{1-x}O_3$, Phys. Rev. B **60**, 11879 (1999).

[57] S. Calder, J. H. Lee, M. B. Stone, M. D. Lumsden, J. C. Lang, M. Feygenson, Z. Zhao, J.-Q. Yan, Y. G. Shi, Y. S. Sun, Y. Tsujimoto, K. Yamaura, and A. D. Christianson, Enhanced spin-phonon-electronic coupling in a 5*d* oxide, Nat. Commun. **6**, 8916 (2015).

[58] C. Cazorla, O. Diéguez, and J. Íñiguez, Multiple structural transitions driven by spin-phonon couplings in a perovskite oxide, Sci. Adv. **3**, e1700288 (2017).

[59] X. Wan, H.-C. Ding, S. Y. Savrasov, and C.-G. Duan, Short range magnetic exchange interaction favors ferroelectricity, Sci. Rep. **6**, 22743 (2016).

[60] B. Xu, Y. M. Dai, L. X. Zhao, K. Wang, R. Yang, W. Zhang, J. Y. Liu, H. Xiao, G. F. Chen, A. J. Taylor, D. A. Yarotski, R. P. Prasankumar, and X. G. Qiu, Optical spectroscopy of the Weyl semimetal TaAs, Phys. Rev. B **93**, 121110(R) (2016).

[61] P. E. C. Ashby and J. P. Carbotte, Chiral anomaly and optical absorption in Weyl semimetals, Phys. Rev. B **89**, 245121 (2014).

[62] G. B. Osterhoudt, Y. Wang, C. A. C. Garcia, V. M. Plisson, J. Gooth, C. Felser, P. Narang, and K. S. Burch, Evidence for Dominant Phonon-Electron Scattering in Weyl Semimetal WP_2, Phys. Rev. X **11**, 011017 (2021).

[63] J. Coulter, G. B. Osterhoudt, C. A. C. Garcia, Y. Wang, V. M. Plisson, B. Shen, N. Ni, K. S. Burch, and P. Narang, Uncovering electron-phonon scattering and phonon dynamics in type-I Weyl semimetals, Phys. Rev. B **100**, 220301(R) (2019).

[64] T. Kim, C. H. Kim, J. Jeong, P. Park, K. Park, K. H. Lee, J. C. Leiner, D. Ishikawa, A. Q. R. Baron, Z. Hiroi, and J.-G. Park, Spin-orbit coupling effects on spin-phonon coupling in $Cd_2Os_2O_7$, Phys. Rev. B **102**, 201101(R) (2020).

[65] B. Cheng, T. Ohtsuki, D. Chaudhuri, S. Nakatsuji, M. Lippmaa, and N. Armitage, Dielectric anomalies and interactions in the three-dimensional quadratic band touching Luttinger semimetal $Pr_2Ir_2O_7$, Nat. Commun. **8**, 2097 (2017).